J. Cent. South Univ. (2022) 29: 645−662
DOI: https://doi.org/10.1007/s11771-022-4908-x

Springer

Numerical simulation on radiation and energy of blast-induced seismic waves in deep rock masses

YANG Jian-hua(杨建华)[1], WU Ze-nan(吴泽南)[1, 2], SUN Wen-bin(孙文彬)[1],
YAO Chi(姚池)[1]*, WANG Qiu-hui(王秋慧)[2]

1. School of Civil Engineering and Architecture, Nanchang University, Nanchang 330031, China;
2. Power China Jiangxi Electric Power Engineering Co., Ltd., Nanchang 330096, China

Abstract: With regard to blasting in deep rock masses, it is commonly thought that an increase in the in-situ stress will change the blast-induced rock crack propagation and ultimately affect rock fragmentation. However, little attention has been given to the change in seismic wave radiation when the fractured zone changes with the in-situ stress. In this study, the influences of in-situ stress on blast-induced rock fracture and seismic wave radiation are numerically investigated by a coupled SPH-FEM simulation method. The results show that the change in blast-induced rock fracture with in-situ stress has a considerable effect on the seismic wave energy and composition. As the in-situ stress level increases, the size of the fractured zone is significantly reduced, and more explosion energy is transformed into seismic energy. A reduction in the size of the fractured zone (seismic wave source zone) results in a higher frequency content of the seismic waves. In a nonhydrostatic in-situ stress field, blast-induced cracks are most suppressed in the direction of the minimum in-situ stress, and thus the seismic waves generated in this direction have the highest energy density. In addition to P-waves, S-waves are also generated when a circular explosive is detonated in a nonhydrostatic in-situ stress field. The S-waves result from the asymmetrical release of rock strain energy due to the anisotropic blast-induced fracture pattern.

Key words: blasting; in-situ stress; seismic wave; rock fracture; SPH-FEM

Cite this article as: YANG Jian-hua, WU Ze-nan, SUN Wen-bin, YAO Chi, WANG Qiu-hui. Numerical simulation on radiation and energy of blast-induced seismic waves in deep rock masses [J]. Journal of Central South University, 2022, 29(2): 645−662. DOI: https://doi.org/10.1007/s11771-022-4908-x.

1 Introduction

Exploitation of deep resources and utilization of deep reservoir space have become common around the world due to the pressures of population growth and the shortage of shallow resources [1−3]. Because of gravity and tectonic movement, deep rock masses are often subjected to high in-situ stress. At present, deep rock excavation in mining and civil engineering is implemented mainly by the drill and blast method, particularly for hard rocks. During rock blasting, the explosion energy is not fully directed into rock fragmentation, and the remaining energy is wasted in the form of light, heat, seismic waves, air blasts, rock ejection and noise. Among these adverse effects, blast-induced seismic waves or vibrations are a major concern for designers and construction workers because such effects can cause damage to nearby structures.

Foundation item: Projects(51969015, U1765207) supported by the National Natural Science Foundation of China; Projects (20192ACB21019, 20181BAB206047) supported by the Natural Science Foundation of Jiangxi Province, China
Received date: 2020-08-12; **Accepted date:** 2021-01-13
Corresponding author: YAO Chi, PhD, Professor; Tel: +86-791-83969657; E-mail: chi.yao@ncu.edu.cn; ORCID: https://orcid.org/0000-0001-9307-9085

Especially in deep openings, high in-situ stress concentrations at local positions cause the rock mass to reach a critical state of failure. Under this scenario, explosion-induced seismic waves, even at low levels, can easily trigger rock failure, and in more severe cases, may result in rockbursts [1, 4, 5]. Therefore, it is very important to minimize explosion-induced seismic waves by properly designing drilling and blasting parameters for deep rock excavation.

With regard to blasting in deep rock masses, it is generally accepted that in-situ stress has a significant effect on blast-induced rock fracture and fragmentation. KUTTER et al [6], YANG et al [7] and QIU et al [8, 9] carried out experimental studies under laboratory conditions to investigate blast-induced crack propagation in uniaxial stress fields. HE et al [10] experimentally studied blast-induced crack propagation in a granite specimen under biaxial confining pressure. Other studies on this topic were conducted by using different numerical modelling methods [11 − 14]. These experimental and numerical studies show that blast-induced cracks propagate preferentially towards the direction in which a higher initial stress is applied, and the final crack lengths are significantly reduced as the initial stress increases. Based on the influences of in-situ stress on blast-induced rock fracture, some blasting design modifications were proposed for deep rock excavation to improve rock fragmentation by blasting. For example, DAI et al [15] suggested reducing the spacing between blastholes and the burden between rows for tunnelling blasts under conditions with high in-situ stress.

During rock blasting, blastholes are filled with detonation products at very high pressures after the detonation of the explosives. This pressure is applied immediately to the blasthole wall and creates an extensively fractured (or crushed) zone and a partially fractured (or cracked) zone surrounding the blasthole, as shown in Figure 1 [16]. Beyond the fractured zone, explosion-induced stress waves continue as elastic seismic waves and cause no further fracture to the rock mass. This region is called the seismic wave zone. In studies of seismic wave radiation from explosives, the blasting source zone and the fractured zone are commonly treated as seismic wave generation zones. Under this treatment, some equivalent pressure is exerted on the outer boundary of the fractured zone to mimic blast loading. Invoking this idea within a dynamic finite element model, BLAIR et al [17] and CHEN et al [18] studied seismic wave radiation from a cylindrical source. AHN et al [19] performed a dynamic finite difference analysis to quantify near-field seismic wave attenuation for a spherical blast source. This equivalent idea was also adopted by SHIN et al [20] and YANG et al [21] to investigate the effects of blast-induced vibration on existing tunnels. Their studies indicate that the size of the fractured zone and the applied equivalent pressure, including its peak and loading frequency, have important effects on the seismic wave radiation.

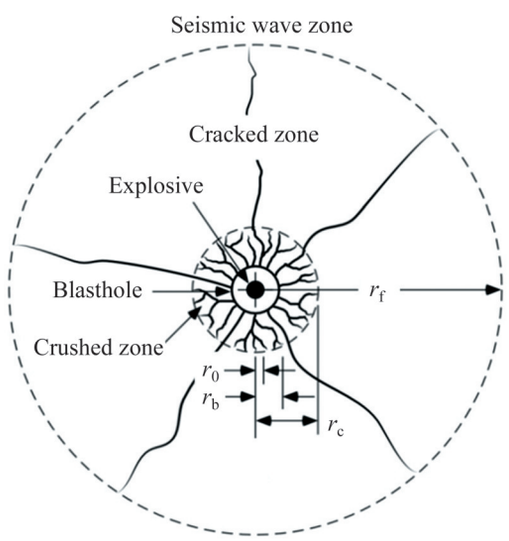

Figure 1 Schematic illustration of seismic wave generation zone around blasthole [16]

In deep rock masses, since a high in-situ stress affects the formation of blast-induced fractures, it will very likely change the seismic wave radiation outside the fractured zone. However, the influence of the change in the fractured zone due to in-situ stress on the seismic wave radiation has not received much attention. In this study, blast-induced rock fracture and seismic wave radiation under different in-situ stress conditions are investigated by using a hybrid SPH-FEM modelling method. Based on numerical simulations, the influences of in-situ stress on the seismic wave energy and composition are analyzed.

2 Numerical method and model

2.1 Coupled SPH-FEM approach

The SPH method is a gridless Lagrangian hydrodynamics method that represents materials as particles. Because the SPH method is free from mesh tangling and hourglass effects, it has some advantages as a numerical tool in modelling problems with large distortions and deformations. Therefore, in recent years, this method has been widely applied to simulate the interaction between explosions and rocks. In the SPH method, the material is represented by arbitrarily distributed particles that carry information such as the particle mass, position and velocity. Using the interpolation theory of kernel approximation, the discrete forms of the mass, momentum and energy conservation equations of the SPH formulation are expressed as follows:

$$\frac{\mathrm{d}\rho_i}{\mathrm{d}t}=\sum_{j=1}^{N}m_j\,(\boldsymbol{v}_j-\boldsymbol{v}_i)\mathrm{A}_{ij} \tag{1}$$

$$\frac{\mathrm{d}\boldsymbol{v}_i^{\alpha}}{\mathrm{d}t}=\sum_{j=1}^{N}m_j\left(\frac{\sigma_j^{\alpha\beta}}{\rho_i^2}A_{ij}-\frac{\sigma_i^{\alpha\beta}}{\rho_j^2}\mathrm{A}_{ij}\right) \tag{2}$$

$$\frac{\mathrm{d}E_i}{\mathrm{d}t}=-\frac{p_i}{\rho_i^2}\sum_{j=1}^{N}m_j\,(\boldsymbol{v}_j-\boldsymbol{v}_i)\mathrm{A}_{ij} \tag{3}$$

where ρ is the density; m is the mass; E is the specific internal energy; t denotes the time; p is the pressure; $\boldsymbol{v}$ is the velocity vector; σ is the stress tensor; subscripts i and j are the particle indices; superscripts α (α=1, 2, 3) and β (β=1, 2, 3) are the space component indices; and A_{ij} is an operator of the interpolating kernel function; which is written as:

$$\mathrm{A}_{ij}=\frac{\boldsymbol{x}_i-\boldsymbol{x}_j}{r_{ij}}\frac{\partial W_{ij}}{\partial r_{ij}} \tag{4}$$

where $\boldsymbol{x}$ is the spatial position vector; r_{ij} is the distance from particle i to particle j; W is the kernel function.

The SPH method was initially developed to address astrophysical problems, such as the modelling of interacting fluid masses in a vacuum without boundaries. When the SPH method is applied to fields other than astrophysics, it cannot enforce finite boundary conditions [22]. Another primary limitation of the current SPH method is its high computational expense, since the computational accuracy is highly dependent on particle refinement. In a one-metre analysis region in rock blast modelling, a discretization consisting of hundreds of thousands or even millions of particles is often required to obtain a satisfactory simulation accuracy. The above difficulties can be avoided by coupling the SPH method with conventional Lagrangian mesh methods such as the FEM. In the coupled SPH-FEM approach, SPH particles are used in the near field where large deformation or severe material failure occurs, and FEM meshes are used in the far field where small deformation is expected. The FEM meshes act as boundaries for SPH particles, and the use of FEM meshes also reduces the high computational cost encountered in the pure SPH method. There are two different ways to enable the coupling interaction between SPH particles and FEM meshes. One is to join SPH particles to corresponding FEM elements through a constraint interface, as shown in Figure 2. The other is not to fasten them together but to allow SPH particles to slide on the surfaces of FEM elements. In this coupling relationship, a special sliding interface algorithm is required [23]. In this study, the joined coupling method is employed here because the interface between the SPH particles and FEM meshes is not a material interface. More details about the coupled SPH-FEM approach can be found in Refs. [22, 23].

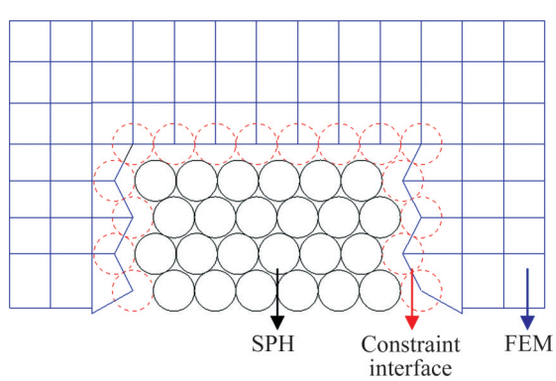

Figure 2 Illustration of coupling between SPH particles and FEM meshes

2.2 Material models

This study numerically simulates a single-hole blast in a stressed homogeneous rock mass by using the nonlinear dynamics software AUTODYN that was first releazed by Century Dynamics. A fully

coupled charge condition in which the blasthole is completely filled with explosives is considered. In this case, only rock and explosive materials are involved in the numerical modelling. Notably, SPH is a Lagrangian technique, and thus when using the coupled SPH-FEM method, the SPH particles can use the same material constitutive model as the FEM elements.

Continuum damage mechanics is often used to describe the material damage process from explosion-induced stress waves [11 − 14]. In this regard, JOHNSON et al [24] proposed a continuum-based damage model (called the JH model) for brittle materials such as rock and ceramic. The JH model is pressure-dependent and strain rate-dependent and hence suitable for modelling high-pressure, large-strain and high-strain-rate problems. After this model was first proposed, it was soon implemented into several codes and widely applied to simulating rock blasts. In the present study, the improved JH-2 constitutive model is adopted to describe the rock material. The JH-2 model consists of a representation of the intact and fractured material strengths, a pressure-volume relationship and a damage model that describes the material evolution from the intact state to the fully fractured state [24]. The evolution from the intact state to a fractured state is represented by a damage scalar D ($0 \leqslant D \leqslant 1.0$). In the intact state ($D$=0), the normalized intact strength σ_i^* is given by:

$$\sigma_i^* = A(P^* + T^*)^N(1 + C\ln\dot{\varepsilon}^*) \tag{5}$$

In the fully fractured state (D=1.0), the normalized residual strength σ_f^* is given as:

$$\sigma_f^* = B(P^*)^M(1 + C\ln\dot{\varepsilon}^*) \tag{6}$$

When the normalized equivalent stresses σ^* exceeds the normalized intact strength σ_i^*, damage begins to occur in the material. As the damage accumulates, the material strength decreases gradually from the intact value σ_i^* to the final residual value σ_f^*. For the damaged material, the normalized equivalent stress for the strength is:

$$\sigma^* = \sigma_i^* - D(\sigma_i^* - \sigma_f^*) \tag{7}$$

where A, N, C, B and M are the material constants; P^* is the normalized pressure; T^* is the normalized maximum tensile hydrostatic pressure that the material can withstand; and $\dot{\varepsilon}^*$ is the normalized strain rate. These strength and stress values are normalized by $\sigma_i^* = \sigma_i/\sigma_{HEL}$, $\sigma_f^* = \sigma_f/\sigma_{HEL}$, $\sigma^* = \sigma/\sigma_{HEL}$, $P^* = P/P_{HEL}$ and $T^* = T/P_{HEL}$, in which σ_i and σ_f are the actual strengths of the intact material and the fully fractured material; σ is the actual equivalent stress; P and T are the actual pressure and the maximum tensile hydrostatic pressure, respectively; and σ_{HEL} and P_{HEL} are the equivalent stress and the pressure at the Hugoniot elastic limit (HEL), respectively. The strain rate is normalized by $\dot{\varepsilon}^* = \dot{\varepsilon}/\dot{\varepsilon}_{ref}$, where $\dot{\varepsilon}$ is the actual equivalent strain rate and $\dot{\varepsilon}_{ref}$ is the reference strain rate, 1.0 s^{-1}.

In the JH-2 model, the hydrostatic pressure P is expressed as a polynomial equation of state (EOS) in terms of volumetric strain μ. For the undamaged material (D=0), the compressive hydrostatic pressure is given by:

$$P = K_1\mu + K_2\mu^2 + K_3\mu^3 \tag{8}$$

where K_1, K_2 and K_3 are material constants. Under tension with μ<0, Eq. (8) is replaced by $P=K_1\mu$. The material damage accumulation results from an increase in pressure. For the damaged material ($0<D\leqslant 1.0$), an incremental pressure ΔP is added to Eq. (8):

$$P = K_1\mu + K_2\mu^2 + K_3\mu^3 + \Delta P \tag{9}$$

The pressure increment is determined from the energy considerations. The hydrostatic potential energy corresponding to the pressure increment is transformed from elastic energy loss due to a decrease in the deviator stress. A fraction ξ ($0 \leqslant \xi \leqslant 1$) is used to quantify the change in energy due to elastic energy loss. More details of the pressure increment ΔP are given in Ref. [24].

The material damage of fracture is considered to be an accumulation of plastic strain, and the damage scalar D is defined as:

$$D = \sum \Delta\varepsilon_p/\varepsilon_p^f \tag{10}$$

where $\Delta\varepsilon_p$ is the increment of the equivalent plastic strain during a cycle of integration; and ε_p^f is the plastic strain required to form a fracture under a constant pressure P. The expression of the fracture strain is:

$$\varepsilon_p^f = D_1(P^* + T^*)^{D_2} \tag{11}$$

where D_1 and D_2 are damage constants.

The constants of the JH-2 model listed in

Table 1 are used in this numerical study [25]. Among these parameters, the density, elastic constants, pressure constants and most strength constants are determined or derived based on laboratory experiments on rock. The strain rate coefficient C=0.005 is assumed to be the same as that of ceramic, which is also a brittle material similar to rock. The damage constants D_1 and D_2 are not directly measurable [25], and numerical adjustments are performed to obtain D_1 and D_2. Different values are numerically tested, and it is found that the values listed in Table 1 can achieve an acceptable fracture pattern. The same approach was also employed by AI et al [25] and DEHGHAN et al [26].

Table 1 Constants of JH-2 model

Parameter		Value
	Density/(kg·m^{-3})	2657
Elastic constant	Elastic modulus/GPa	80
	Shear modulus/GPa	31
	Bulk modulus, K_1/GPa	55.6
Strength constant	Hugoniot elastic limit (HEL)/GPa	4.5
	HEL equivalent stress/GPa	2.66
	HEL pressure/GPa	2.73
	Hydrostatic tensile limit/GPa	0.15
	Intact strength coefficient, A	1.01
	Intact strength exponent, N	0.83
	Strain rate coefficient, C	0.005
	Fractured strength coefficient, B	0.68
	Fractured strength exponent, M	0.76
	Normalized maximum fracture strength	0.2
Pressure constant	Pressure constant, K_2/GPa	−23
	Pressure constant, K_3/GPa	2980
	Bulking factor	1.0
Damage constant	Damage coefficient, D_1	0.01
	Damage exponent, D_2	0.9

The AUTODYN program is a general-purpose engineering software package that uses finite difference, finite volume, and finite element techniques to solve a wide variety of nonlinear problems in solid, fluid and gas dynamics. It is one of the few programs that can be used to simulate explosive detonation and explosive-structure interaction. In AUTODYN, the simulation of explosion is commonly implemented by the Jones-Wilkins-Lee (JWL) EOS. The JWL equation defines the pressure of detonation products P_d as:

$$P_d = C_1\left(1-\frac{\omega}{R_1V}\right)e^{-R_1V} + C_2\left(1-\frac{\omega}{R_2V}\right)e^{-R_2V} + \frac{\omega E_{se}}{V} \tag{12}$$

where V is the relative specific volume; E_{se} is the specific energy; and C_1, C_2, R_1, R_2 and ω are explosive constants that are determined by dynamic experiments.

2.3 Numerical model

Cylindrical blastholes that measure 2 − 5 m in length are typically used in blasting excavation of deep tunnels. In principle, a three-dimensional (3D) blasthole and rock mass model is required to numerically investigate the influence of in-situ stress on blast-induced rock fracture and seismic wave radiation. In dynamic FEM modelling, in order to guarantee the resolution of the high-frequency waves near the explosive columns, a uniform element size smaller than 5 mm is needed to avoid any wave distortion [27]. Under this requirement, a 3D model that covers a 5 m span will be discretized into at least one billion elements to achieve uncontaminated waves. This is too time-consuming at the current computational level, particularly for performing the in-situ stress initialization modelling. For this reason, it is assumed that the explosion pressure is uniformly distributed along the blasthole axis, and the explosive detonation in a blasthole is simplified to a plane strain problem. To highlight the effect of in-situ stress, the rock is considered as a homogeneous and isotropic material.

Figure 3 shows the geometry of the numerical model developed with AUTODYN. The entire analysis region is a 4 m×4 m area. A blasthole with a diameter of 40 mm is arranged in the centre of the model. As mentioned previously, a fully coupled charge is used in the present study, and the explosive diameter is equal to the blasthole diameter. Horizontal pressure σ_x and vertical pressure σ_y are preloaded on the outer boundaries of the model to mimic an in-situ stress field. Many experimental and numerical studies show that the radius of the extensively fractured zone around a blasthole is approximately 2 − 10 times the blasthole radius [12, 28]. To improve computational

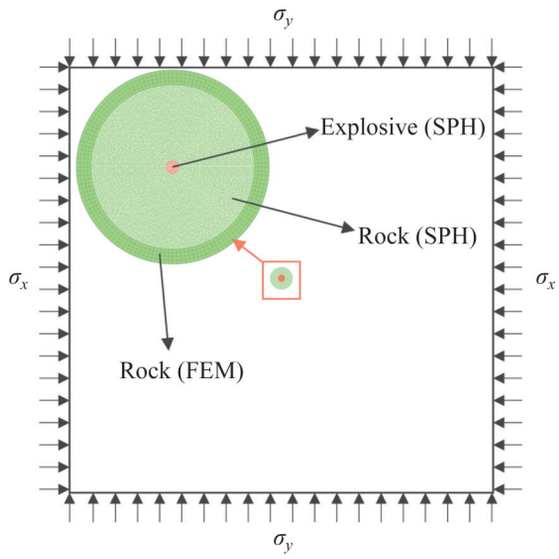

Figure 3 Analytical model of numerical simulation

efficiency, the explosive and the rock within 10 times the blasthole radius are simulated with SPH particles, and the rock outside this radius is simulated by using FEM meshes. It is well known that the accuracy of the dynamic FEM simulation is highly dependent on the mesh refinement. According to existing studies [21, 27], 6 − 12 elements per wavelength are required to avoid any wave distortion. In this SPH-FEM modelling, the lowest wave velocity (Rayleigh wave velocity) of the rock material is 3210 m/s. The highest frequency of the explosion-induced seismic waves is approximately 100 kHz (see the amplitude-frequency spectra in Section 4.1). Consequently, the shortest wavelength of interest is estimated to be 0.03 m. According to the above mentioned requirement, the element size near the blasthole should be smaller than 2.5−5.0 mm. As the distance from the blasthole increases, the amplitude at high frequency decreases. Therefore, a gradient FEM mesh is adopted in this numerical study. In the process of determining the mesh refinement, numerical convergence tests are performed. The element size is gradually reduced until the difference in the modelling results between two consecutive tests is less than 5%. Finally, the gradient FEM mesh in which the element size varies from 1 mm near the blasthole to 5 mm at the model borders is used in this study. Accordingly, the spacing between the adjacent SPH particles is set to 0.5 mm.

In this study, both hydrostatic and nonhydrostatic in-situ stress fields are considered to fully investigate the influence of in-situ stress on explosion-induced seismic wave radiation. For the hydrostatic in-situ stress fields, the stress levels vary from 0 to 60 MPa (0, 10, 20, 30 and 60 MPa). The in-situ stress test results show that the vertical in-situ stress σ_y approximates the gravity stress of the overburden rock mass, i.e., $\sigma_y=\gamma H$, where γ is the unit weight of the rock mass and H is the depth below the surface. The ratio of the average horizontal in-situ stress $\sigma_{x,\mathrm{av}}$ to the vertical in-situ stress σ_y follows the relationship $(100/H+0.3)\leqslant \sigma_{x,\mathrm{av}}/\sigma_y\leqslant (1500/H+0.5)$ [29]. According to this law, when the vertical in-situ stress σ_y is equal to 10 MPa, the depth H is approximately 376 m, and the ratio $\sigma_{x,\mathrm{av}}/\sigma_y$ varies in the range from 0.6 to 4.5. Therefore, in this study, the vertical in-situ stress σ_y=10 MPa and the stress ratios σ_x/σ_y=2.0 and σ_x/σ_y=3.0 are considered as typical nonhydrostatic in-situ stress fields. Numerical modelling of blasting in a stressed rock mass involves two steps, static stress initialization and blast loading. The horizontal and vertical in-situ stresses are first exerted on the outer boundaries of the model. After the rock mass system becomes stable under the static in-situ stress, detonation of the explosive is initiated.

2.4 Verification of numerical method and model

JUNG et al [30] performed single-hole blasting tests on marble slabs in a laboratory. In these tests, the marble slabs with dimensions of 200 mm× 200 mm×23 mm were employed. A circular hole with a diameter of 8 mm was drilled in the centre of the marble slabs. The marble material had a density of 2625 kg/m^3, an elastic modulus of 20.7 GPa, a Poisson ratio of 0.12 and a tensile strength of 6.2 MPa. Two types of tests were conducted in their experimental work: testing without prestress and testing with a uniaxial stress of 5 MPa preloaded on the slabs before blasting. Blasting is implemented by using high-precision detonators. The blast-induced rock fracture modes under no prestress and a uniaxial prestress of 5 MPa are shown in Figure 4.

To verify the numerical method and model, we numerically replicate the single-hole blasting tests conducted by JUNG et al [30] with the coupled SPH-FEM method. The sizes, rock parameters and

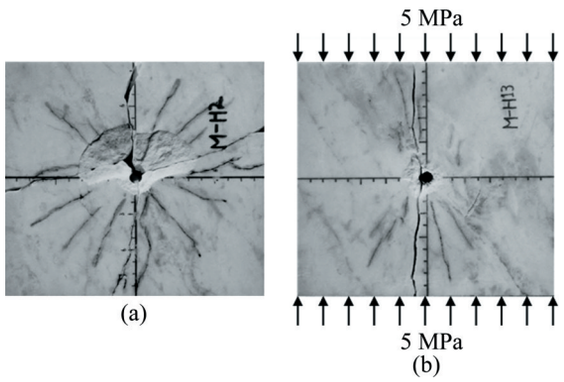

Figure 4 Photographs of marble slabs after blasting: (a) Without prestress; (b) Under a uniaxial prestress of 5 MPa [30]

prestress conditions of the numerical models remain identical to those of the specimens used in the tests. The JWL EOS is used to simulate the blasting effect in the marble slabs. The constants adopted for the JWL EOS of the detonation products are summarized in Table 2. The simulated rock fracture patterns caused by blasting under no prestress and a uniaxial prestress are presented in Figure 5. Both the experimental and numerical results show that when no prestress is applied, the blast-induced cracks propagate radially around the borehole. However, when a uniaxial prestress of 5 MPa is exerted, the crack propagation is directional, aligning with the prestress direction. The longest crack length observed in the numerical simulations also agrees well with that observed in the tests. The agreement between the numerical simulation results and the experimental observations indicates that the SPH-FEM method and the numerical model are suitable for simulating blast-induced rock fracture, whether in the presence or absence of prestress.

Table 2 Explosive constants used in JWL EOS

Parameter	Value
Density/(kg·m^{-3})	1630
Velocity of detonation/(m·s^{-1})	6930
Chapman-Jouguet pressure/GPa	21
C_1/GPa	373.77
C_2/GPa	3.747
R_1	4.15
R_2	0.90
ω	0.35
CJ energy unit volume/(kJ·m^{-3})	6.0×10^6

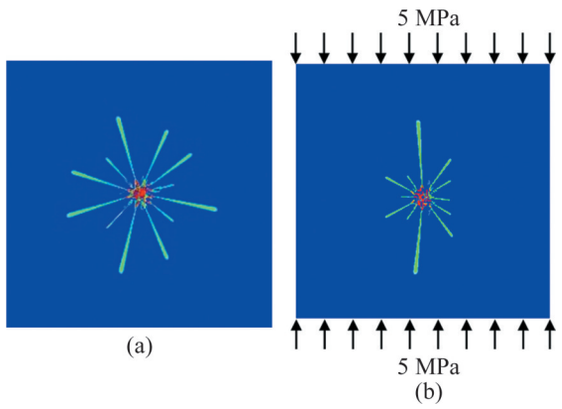

Figure 5 Numerical simulation results of single-hole blasting in marble slabs: (a) Without prestress; (b) Under uniaxial prestress of 5 MPa

3 Blast-induced rock fracture under in-situ stress conditions

As mentioned earlier, the blasting source and the blast-induced fractured zone are usually treated as the source zone of explosion-induced seismic wave radiation so that elastic wave theory can be applied to this problem. Therefore, to elucidate the influence of in-situ stress on seismic wave radiation, it is necessary to first investigate blast-induced rock fracture under in-situ stress conditions.

3.1 Hydrostatic in-situ stress conditions

Figure 6 presents the distributions of the blast-induced rock fractures at 0.05, 0.2 and 0.5 ms after explosive detonation under different hydrostatic in-situ stress levels. Within 5 times the blasthole radius, the rock mass is extensively fractured, and a crushed zone is created in the immediate vicinity of the blasthole. The crushed zone is followed by a cracked zone, in which the radial crack density is lower and the rock mass is partially fractured. However, the size of the cracked zone is much larger than that of the crushed zone. The fracture pattern simulated in this study agrees well with the experimental observations presented in Refs. [26, 28]. Notably, in the present numerical simulation, the explosive and rock materials are considered to be homogeneous and isotropic, and the in-situ stress is uniformly distributed around the blasthole. However, these ideal conditions are difficult to guarantee during laboratory testing and engineering practice. Therefore, in experimental studies, the

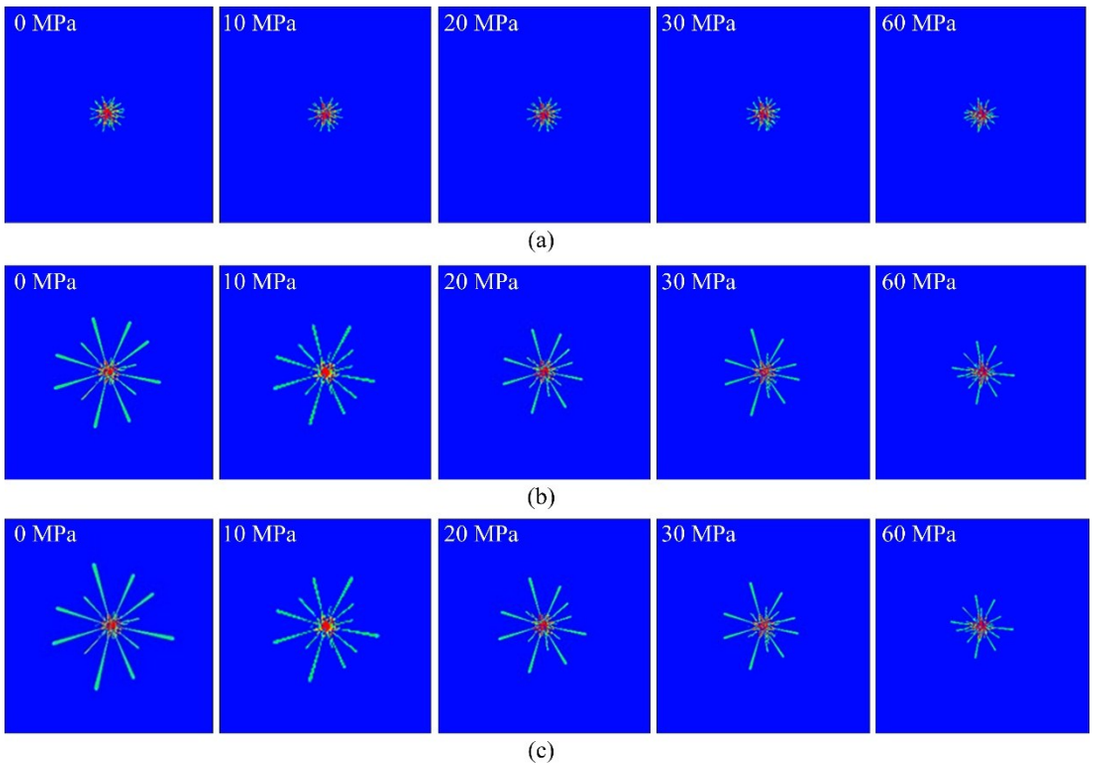

Figure 6 Blast-induced rock fracture under different hydrostatic in-situ stress levels: (a) 0.05 ms; (b) 0.2 ms; (c) 0.5 ms

longest crack often propagates along a certain direction. It is generally accepted that the crushed zone is created by shear stress due to the intense compressive stress acting on the blasthole wall and that the cracked zone is caused by circumferential tensile stress [12]. At different in-situ stress levels, the crushed zones have approximately equal sizes (5 times the blasthole radius) and are completely formed at almost the same time (0.05 ms). This indicates that the in-situ stress has little effect on the formation of the crushed zone because the in-situ stress is much lower than the explosion pressure.

In the cracked zone, the cracks are radially distributed, and the final crack lengths become significantly shorter as the in-situ stress increases. This is because the radial cracks are created by the circumferential tensile stress, and the tensile effect is neutralized by the compressive in-situ stress. The explosion-related tensile stress decays with increasing distance. When it decays to a level that is insufficient to overcome the tensile strength of the rock mass under a compressive in-situ stress, radial crack propagation stops. The distance from the tip of the longest crack to the blasthole centre is defined as the fractured zone radius r_f (see Figure 1). Consequently, the area of the fractured zone, which includes the crushed zone and the cracked zone, can be calculated by $A_f = \pi(r_f^2 - r_b^2)$, where r_b is the blasthole radius. Figure 7 shows the variations in the fractured zone radius and the fractured zone area with time under different in-situ stress levels. Within 0.05 ms, the area of the fractured zone is approximately consistent for different in-situ stress levels. This is because in the first 0.05 ms, the in-situ stress has little effect on the formation of the crushed zone. After 0.05 ms, the area of the fractured zone begins to vary under different in-situ stress levels. The fractured area decreases as the in-situ stress level increases. The final area of the fractured zone at σ_x=σ_y=60 MPa is only 24.6% of that in the absence of in-situ stress. Furthermore, after 0.05 ms, the crack propagation velocity slows with an increase in the in-situ stress level, as shown in Figure 8. At σ_x= σ_y=0 MPa, the cracks continue to grow for 0.45 ms. At σ_x= σ_y= 60 MPa, the cracks stop spreading as early as 0.20 ms. At t=0.15 ms, the crack propagation velocity for the σ_x= σ_y=0 MPa case can reach 2180 m/s. At the same time, the cracking velocity under σ_x=σ_y=60 MPa is 120 m/s, which is only 5.5% of the former.

The above analysis indicates that the presence

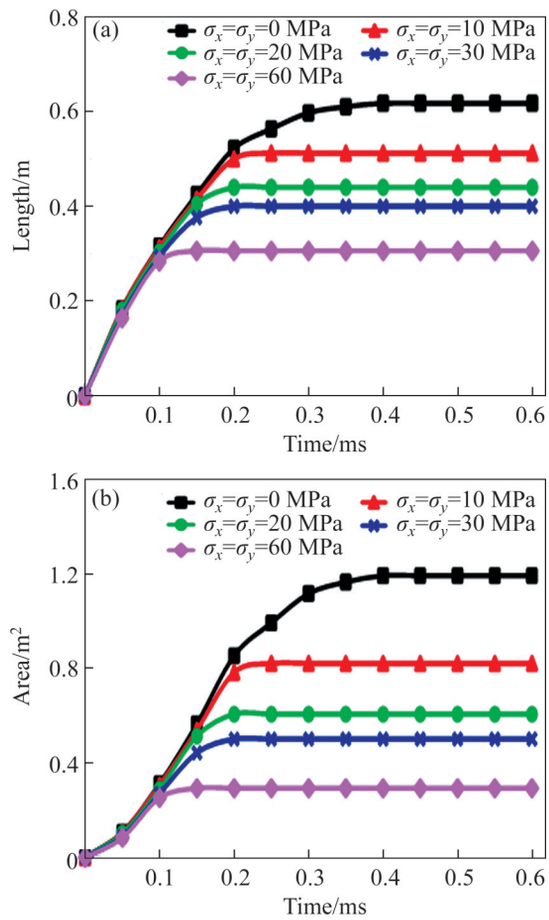

Figure 7 Variation in fractured zone with time under different hydrostatic in-situ stress levels: (a) Fracture length; (b) Fractured zone area

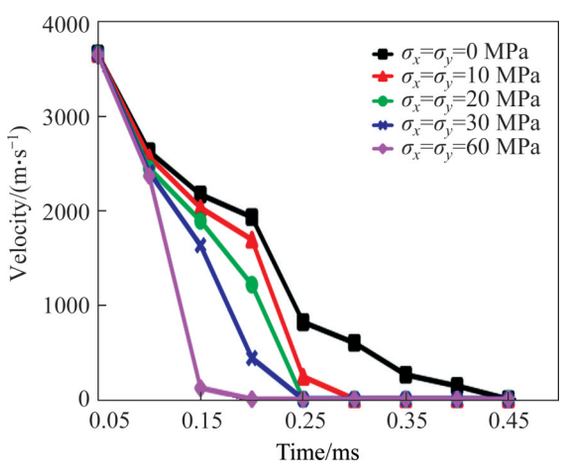

Figure 8 Variation in crack propagation velocity with time under different hydrostatic in-situ stress levels

of in-situ stress has a considerable suppression effect on explosion-induced rock fracture. More specifically, the suppression is mainly manifested in the middle and later stages of explosion and reduces the length of the radial cracks. This effect may explain the difficulty in implementing presplit blasting in deep rock masses with high in-situ stresses. In this situation, the smooth blasting method is a better option. To achieve the same fragmentation as that achieved in shallow rock masses, a greater specific charge is required with respect to the production blasting in deep rock masses. Another choice for this purpose is to use explosives that have higher densities and higher velocities of detonation to properly increase the explosion pressure. However, these measures for improving rock fragmentation also increase the risk of damage to the remaining rock masses. Under this scenario, the charge in stoping rows and buffer rows needs to be cautiously designed so that the damage from all of the blastholes will not exceed the damage created by the final contour row.

Rock fracture caused by blasting is a complicated and dynamic process. The extents of the crushed zone and the cracked zone are influenced by many factors, including explosive type, rock mass properties and blasting parameters. Therefore, the extents of the crushed zone and the cracked zone reported by different researchers are quite different. A review of the existing studies with regard to single-hole blasting tests in a free field without in-situ stress indicates that the crushed zone radius varies within 2−10 times the blasthole radius and that the cracked zone radius varies within 10−150 times the blasthole radius [8, 9, 26, 28, 30]. These ranges are wide and consequently pose a challenge in accurately predicting the extents of the crushed zone and the cracked zone. In the present numerical study under σ_x= σ_y=0 MPa, the crushed zone radius of r_c=5r_b and the cracked zone radius of r_f=30r_b are obtained. These results fall within the range of the experimental observations. In engineering practices, acoustic tests and borehole televiewer scans show that blast-induced cracks (rock damage) can extend 2−3 m into the surrounding rock mass [4]. It is much longer than the length of the cracks caused by the single-hole blasts. This is because practical engineering blasts involve multiple blastholes and excavation cycles, and the cracks will continue to grow under repeated blast loading. Furthermore, natural rock masses contain many initial cracks. Under blast loading, the propagation of initial cracks occurs more easily than the formation of new cracks.

3.2 Nonhydrostatic in-situ stress conditions

Figure 9 shows the formation processes of blast-induced rock fractures under the nonhydrostatic in-situ stress fields σ_x=2σ_y=20 MPa and σ_x=3σ_y=30 MPa. Similarly, before t=0.05 ms, the cracks first propagate synchronously around the blasthole, without being affected by the nonhydrostatic in-situ stress. The size of the crushed zone created in the nonhydrostatic in-situ stress fields is almost the same as that in the hydrostatic in-situ stress fields, approximately 5 times the blasthole radius. After t=0.05 ms, the cracks tend to grow along certain directions, and the final fractured zone has an elliptical shape. The major axis of the elliptical fractured zone is in the direction of the maximum in-situ stress, and the minor axis corresponds to the minimum in-situ stress orientation. As explained earlier, the radial cracks are caused by the explosion-induced tensile stress in the circumferential direction. Under the nonhydrostatic in-situ stress conditions with σ_x/σ_y>1.0, the circumferential compressive stress is minimal at polar angles of 0° and 180°, and reaches a maximum at polar angles of 90° and 270°. Therefore, in theory, the radial tensile cracks spreading along the maximum in-situ stress orientation encounter the weakest suppression from the in-situ stress. In contrast, the strongest suppression is experienced by the cracks propagating along the minimum in-situ stress orientation. For the elliptical fractured zone, the ratio of the major axis to the minor axis is 1.68 at σ_x=2σ_y=20 MPa, and this ratio is 2.07 in the case of σ_x=3σ_y=30 MPa. The anisotropy of the fractured zone becomes more apparent as the difference between the horizontal in-situ stress σ_x and the vertical in-situ stress σ_y increases.

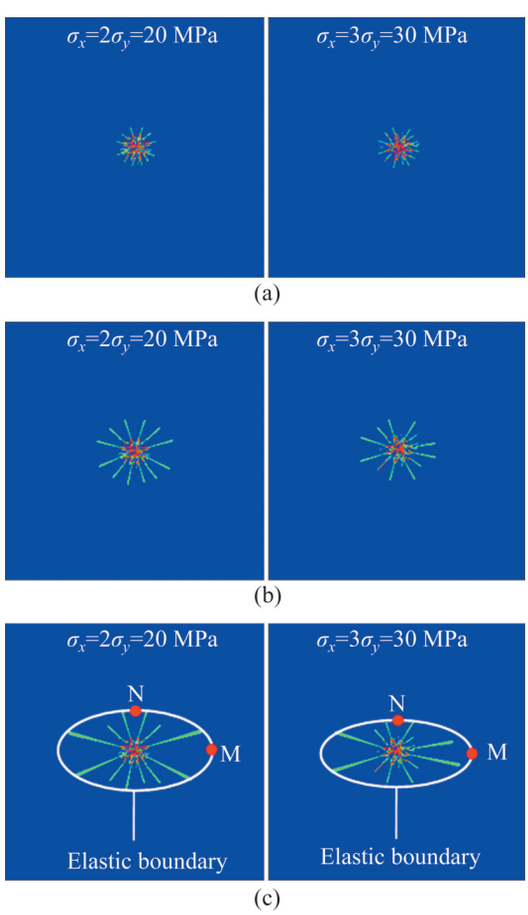

Figure 9 Blast-induced rock fracture under nonhydrostatic in-situ stress conditions: (a) 0.05 ms; (b) 0.2 ms; (c) 0.5 ms

It should be noted that in the numerical simulation results, the longest (shortest) crack does not appear precisely in the direction of the maximum (minimum) in-situ stress. There is a small angle between the propagation direction of the longest (shortest) crack and the maximum (minimum) in-situ stress orientation. This is because in the coupled SPH-FEM modelling, the explosive and the rock in the immediate vicinity of the blasthole are discretized into arbitrarily distributed SPH particles, as shown in Figure 3. Under a limited number of particles, the distribution of the particles is not completely centrosymmetric to the blasthole centre. In this circumstance, the particle motion under the single explosion action is also not completely centrosymmetric around the blasthole, which does not fit the theoretical model perfectly. Therefore, the numerical simulation results deviate slightly from the theoretical analysis. The same phenomenon was observed in other numerical simulations carried out by different authors [11, 25, 26]. Nevertheless, the overall elliptical distribution of the fractured zone agrees well with the theoretical analysis.

The numerical results in Figure 9 show that the nonhydrostatic in-situ stress affects the blasting fracture orientation. This is consistent with the experimental observations reported in the literature [6−10, 30]. From another perspective, the anisotropic blasting fracture pattern may provide an approach to estimate the principal in-situ stress orientations in a plane. The major axis of the elliptical fractured zone and its inclination

correspond to the maximum in-situ stress orientation orthogonal to the blasthole axis. Furthermore, based on the above analysis, arranging blastholes along the maximum in-situ stress orientation will facilitate crack connection between adjacent blastholes and thus increase rock fragmentation and create smooth free faces.

4 Blast-induced seismic waves under in-situ stress conditions

During rock blasting, a portion of the explosion energy is converted into mechanical energy applied to the surrounding rock masses. Among the mechanical energy sources, some of this energy is effectively used to break rock masses and eject rock fragments, and the rest produces undesired seismic waves. Since rock fragmentation is considerably affected by in-situ stress, the seismic wave energy, as a part of the mechanical energy, will probably change under the action of in-situ stress. The ratio of the seismic energy to the total explosion energy, also called the seismic efficiency, is an important indicator of blasting quality and safety evaluation in rock blasting engineering. Furthermore, in nonhydrostatic in-situ stress fields, the anisotropic blasting fracture pattern corresponds to an anisotropic seismic wave source, which may result in different wave compositions from those in free or hydrostatic in-situ stress fields. This section investigates the energy and composition of blast-induced seismic waves under hydrostatic and nonhydrostatic in-situ stress conditions. Notably, in the present numerical investigation, only the mechanical energy carried by the explosive stress wave is considered, and the mechanical energy in the form of explosive gas flow is not considered.

4.1 Hydrostatic in-situ stress conditions

The energy transferred to the rock mass in the form of seismic waves can be calculated as the integral of energy flow past a control surface in the direction along the normal external vector $\boldsymbol{n}$ [31]:

$$E_s = \int_s \int_t \boldsymbol{\Phi} \cdot \boldsymbol{n} \mathrm{d}t \mathrm{d}S \tag{13}$$

where E_s is the seismic wave energy; S is the area of the control surface; t is the time; and $\boldsymbol{\Phi}$ is the energy flux vector whose modulus represents the power or rate of work per unit area. $\boldsymbol{\Phi}$ is determined by the scalar product of the stress vector $\boldsymbol{\sigma}$ and the particle velocity vector $\boldsymbol{v}$:

$$\boldsymbol{\Phi} = \boldsymbol{\sigma} \cdot \boldsymbol{v} \tag{14}$$

For different hydrostatic in-situ stress levels, Figure 10(a) shows the time histories of the seismic energy flux transmitted through the outer boundary

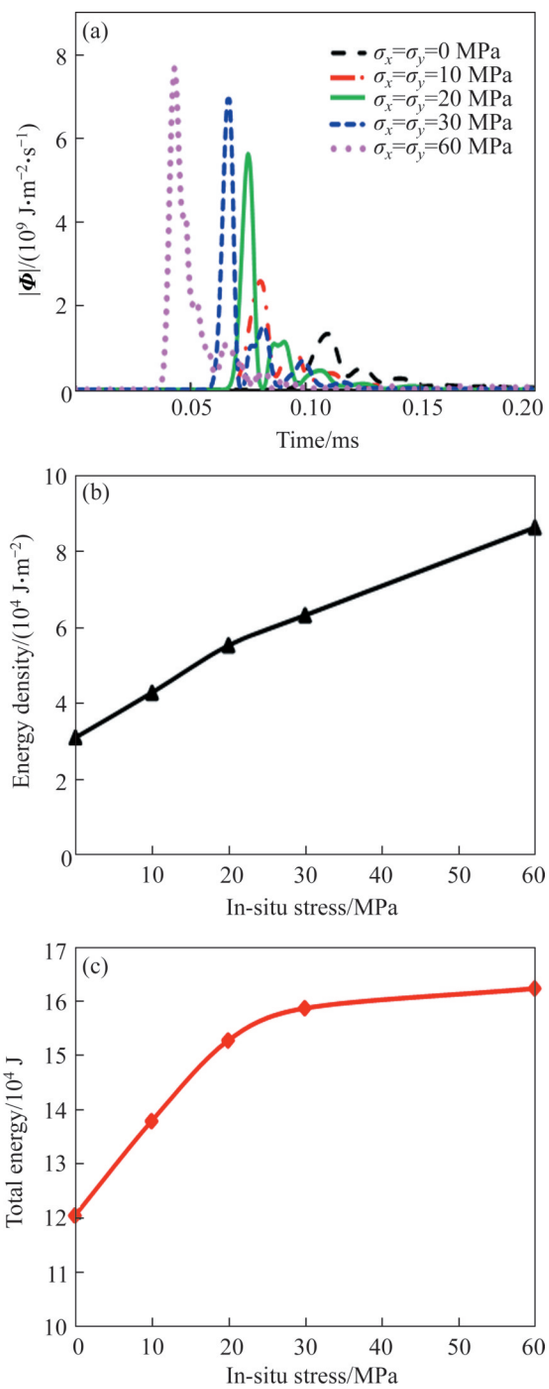

Figure 10 Explosion-induced seismic wave energy under different hydrostatic in-situ stress levels: (a) Time histories of energy flux; (b) Energy density; (c) Total energy

of the fractured zone (elastic boundary) in the normal direction. In the free field without in-situ stress, the maximum seismic energy flux is 1.34×10^9 J/(m^2 · s), attained at 0.11 ms. Under the stress condition $\sigma_x=\sigma_y$=60 MPa, the seismic energy flux reaches a peak of 7.69×10^9 J/(m^2 · s) at 0.043 ms. According to Eq. (13), integrating the seismic energy flux in Figure 10(a) over time gives the seismic energy per unit area, i.e., the energy density. The seismic energy density is of practical significance because it corresponds to the vibration intensity at an observation point. Under $\sigma_x=\sigma_y$= 60 MPa, the seismic energy density is 8.62×10^4 J/m^2, which is 2.8 times the value under $\sigma_x=\sigma_y$= 0 MPa, as shown in Figure 10(b). In the planar case of this study, the total seismic energy is the integral of the energy density over the entire area of the elastic boundary with a unit thickness. With an increase in the in-situ stress, the area of the elastic boundary is reduced. Then, the total seismic energy under $\sigma_x=\sigma_y$=60 MPa becomes 1.3 times the total seismic energy at $\sigma_x=\sigma_y$=0 MPa (see Figure 10(c)). The quantitative comparison shows that the energy of blast-induced seismic waves will increase as the in-situ stress level increases. This is because under a greater in-situ stress, the fractured zone is significantly reduced and consumes less energy, and hence more explosion energy is transferred to the rock mass in the form of seismic waves.

Since the size of the fractured zone or the seismic source zone decreases under the action of in-situ stress, the frequency of the seismic waves generated on the elastic boundary will increase with the in-situ stress. As shown in Figure 11, the normalized Fourier spectrum shifts to higher frequencies with increasing in-situ stress level. In Figure 11, A is the current value of the amplitude, and A_{max} is its maximum value. To facilitate the comparison of the frequency content, the analysis is carried out in terms of the mean frequency calculated from the following formula [32]:

$$f_m=\frac{\sum f_i\cdot A(f_i)}{\sum A(f_i)} \tag{15}$$

where f_m is the mean frequency; f_i is the individual frequency in the spectrum; and $A(f_i)$ is the amplitude associated with each frequency f_i.

The mean frequency of the Fourier spectrum is

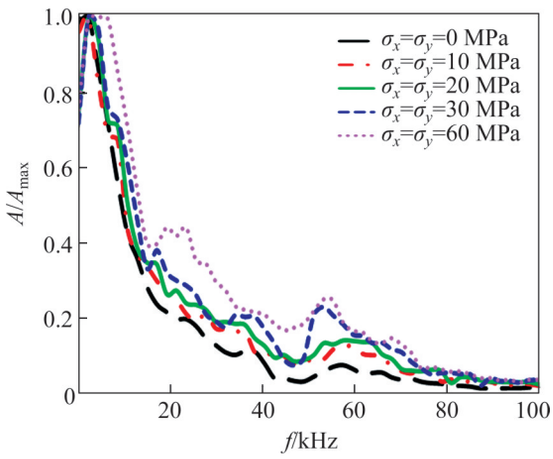

Figure 11 Normalized amplitude-frequency spectra of explosion-induced seismic waves on elastic boundary

18.02 kHz for the case $\sigma_x=\sigma_y$=0 MPa. At $\sigma_x=\sigma_y$= 60 MPa, the mean frequency on the elastic boundary reaches 25.78 kHz, 1.43 times that of the former. It is well known that seismic wave attenuation is frequency-dependent and that amplitudes at high frequencies decay faster than amplitudes at low frequencies. Therefore, with regard to blasting under high in-situ stress conditions, a higher initial seismic energy in the source zone will not necessarily result in a greater vibration amplitude far from the blasthole.

In geophysical laws, the reduction in seismic wave amplitude is attributed to viscoelastic attenuation and geometric spreading. The viscoelastic attenuation is generally specified by the quality factor Q. Laboratory measurements show that the value of Q is related to the level of in-situ stress [33, 34]. When the in-situ stress acting on a rock mass increases, the microfissures in the rock mass tend to close, which results in an increase in the quality factor Q. Q will gradually stabilize at a constant as the in-situ stress increases. However, when the in-situ stress reaches a level that is high enough to cause microfissure growth or generate new cracks, the quality factor Q will decrease [33]. From the perspective of the seismic source size and the quality factor, the influence of in-situ stress on the attenuation of explosive seismic waves is very complicated. The present study only investigates the influence of in-situ stress on the generation of explosive seismic waves, and the wave attenuation under in-situ stress conditions is beyond the scope of this paper.

4.2 Nonhydrostatic in-situ stress conditions

Figure 12 shows the time histories of the seismic energy flux observed at points M and N (see Figure 9(c)) under the nonhydrostatic in-situ stress conditions σ_x=2σ_y=20 MPa and σ_x=3σ_y=30 MPa. Observation points M and N are both located at the elastic boundary. Point M is aligned with the direction of the maximum in-situ stress, and point N is aligned with the direction of the minimum in-situ stress. Since the presence of a nonhydrostatic in-situ stress changes the blasting fracture orientation, the explosion-induced seismic waves on the outer boundary of the fractured zone also exhibit anisotropy. The seismic energy density at the observation point aligned with the minimum in-situ stress orientation is distinctly higher than that aligned with the maximum in-situ stress direction. This is because under the suppression of the nonhydrostatic in-situ stress, the extent of the rock fracture in the direction of the minimum in-situ stress is smaller. Therefore, in this direction, the rock fracture consumes less explosion energy, and then more energy is converted into seismic energy. At σ_x=2σ_y=20 MPa, the ratio of the seismic energy density between points N and M is 1.79. This ratio is 1.90 for the in-situ stress condition σ_x=3σ_y= 30 MPa. The anisotropy of the seismic energy density also becomes more obvious as the difference between the principal in-situ stresses increases.

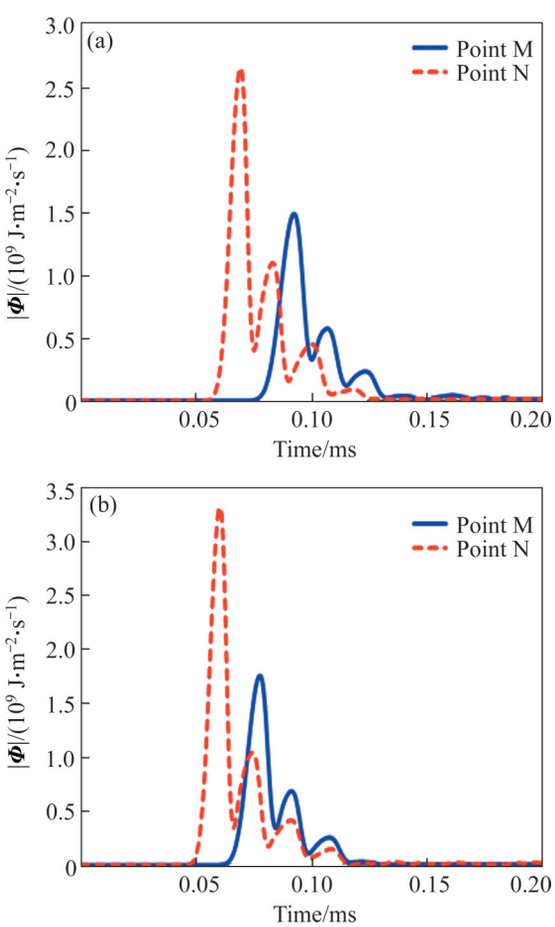

Figure 12 Seismic energy flux under nonhydrostatic in-situ stress conditions: (a) σ_x=2σ_y=20 MPa; (b) σ_x=3σ_y= 30 MPa

Figure 13 presents the resultant velocity histories observed at the same distance from the elastic boundary under different in-situ stress conditions σ_x=σ_y=0 MPa, σ_x=σ_y=10 MPa and σ_x=2σ_y= 20 MPa. The three cases represent a free field without in-situ stress, a hydrostatic in-situ stress field and a nonhydrostatic in-situ stress field. The observation point is located at a 90° polar angle along the minimum in-situ stress orientation, and the distance to the elastic boundary is 0.2 m. In the free field and the hydrostatic in-situ stress field, the composition of the blast-induced seismic waves is the same, with only P-waves. Under the nonhydrostatic in-situ stress condition, after the first arriving P-wave, another wave that has a smaller amplitude reaches the observation point at approximately 0.19 ms. However, this wave does not clearly appear in the free and hydrostatic in-situ stress fields. According to the elastic constants used in the numerical modelling, the velocity of the S-waves travelling through the rock mass is approximately 3416 m/s. Actually, the S-wave velocity will be slightly greater than this value when the compressive in-situ stress is considered. At this speed, it takes approximately 0.18 ms for the seismic S-waves to reach the observation point

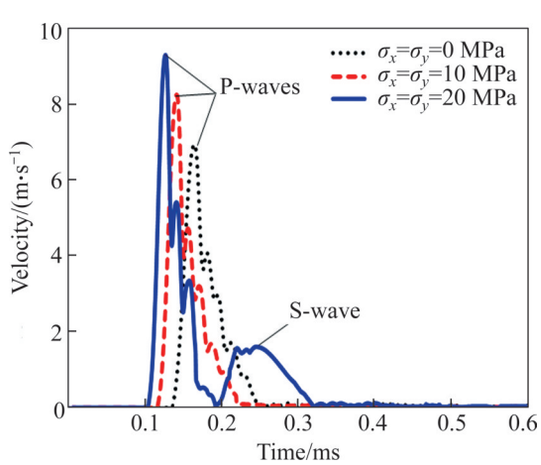

Figure 13 Resultant velocity histories under different in-situ stress conditions

0.6 m from the blasthole centre. From the time of arrival, it can be inferred that the wave that arrives later in the nonhydrostatic in-situ stress field is the S-wave.

Theoretically, a circular explosion source in a homogeneous and isotropic medium should not generate any S-waves unless there are differential movements that occur due to the explosion. Under free and hydrostatic in-situ stress conditions, the blast-induced rock fracture and movement along cracks would be uniformly distributed with radial symmetry around the blasthole centre. Therefore, under these conditions, an S-wave radiation pattern is not expected. Notably, with regard to blasting in a stressed rock mass, a part of the stored strain energy is instantaneously released due to blast-induced rock fracture. The strain energy stored in the zone that is fractured is released, and the strain energy outside the fractured zone is reduced. Some theoretical and experimental studies have demonstrated that the rapid release of strain energy can also trigger seismic waves [35, 36]. In a nonhydrostatic in-situ stress field, blast-induced cracks preferentially spread in the direction where the circumferential compressive stress is minimal. This anisotropic fracture pattern causes the rock strain energy around the blasthole to be released asymmetrically, resulting in S-wave radiation. The radiation pattern of seismic waves due to an induced rupture in a prestressed medium was studied by ARCHAMBEAU [37], and he found that the S-wave radiation could be represented by a symmetric quadrupole source.

Since the rapid release of rock strain energy in the nonhydrostatic in-situ stress field contributes to the S-wave radiation, the amplitude of the S-waves will vary with the in-situ stress conditions. At σ_x=$2\sigma_y$=20 MPa, the peak of the S-wave is 1.61 m/s at a distance of 0.2 m from the elastic boundary. When the preloaded stress reaches σ_x=$2\sigma_y$=40 MPa, the S-wave peak at the same distance becomes 2.60 m/s, 1.61 times the former, as shown in Figure 14. Under nonhydrostatic in-situ stress conditions, the rock strain energy density in the direction of the minimum in-situ stress is the highest due to the existence of the blasthole cavity. Therefore, the S-wave observed at the point in this direction has a greater amplitude. As can be seen in Figure 15(a), under σ_x=$2\sigma_y$=20 MPa, the peak of the S-wave at 0.2 m from the elastic boundary in the minimum in-situ stress orientation is 87.2% higher than the peak observed at the same distance in the direction of the maximum in-situ stress. Furthermore, the difference in the S-wave amplitude

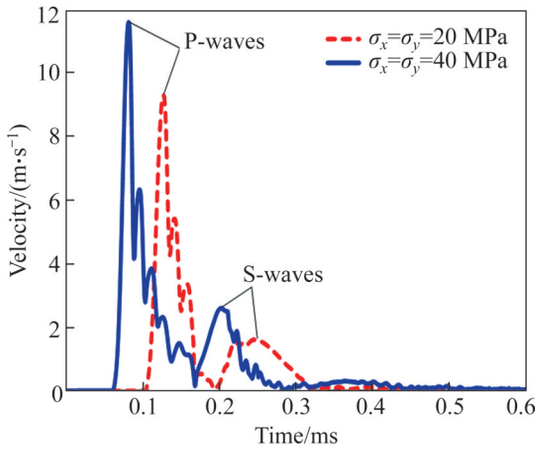

Figure 14 Comparison of S-waves under different nonhydrostatic in-situ stress levels

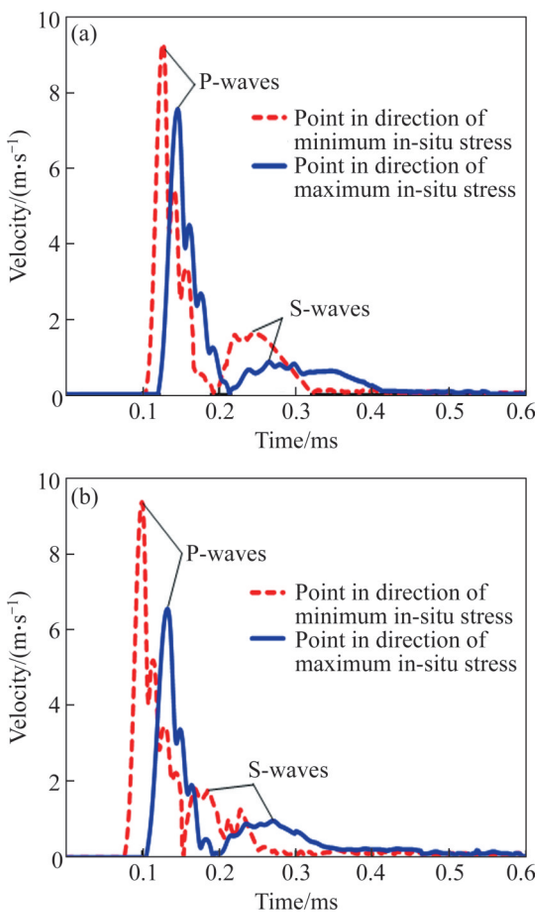

Figure 15 Comparison of the S-waves observed at the points in the maximum and minimum in-situ stress directions under: (a) σ_x=$2\sigma_y$=20 MPa; (b) σ_x=$3\sigma_y$=30 MPa

between the two principal in-situ stress directions becomes larger as the principal stress ratio σ_x/σ_y increases. As shown in Figure 15(b), the difference in the amplitude reaches 139.6% under $\sigma_x=3\sigma_y=$ 30 MPa.

Although the S-waves are generated by only the release of rock strain energy, the P-waves contain different components due to two sources, i. e., explosion energy and rock strain energy. It is not easy to distinguish and separate the fraction due to the strain energy release alone unless the functions describing the spatiotemporal distributions of the two sources are exactly known. LU et al [38] estimated the duration of the strain energy release occurring at blast-created excavation boundaries by analysing the rock fracture process between adjacent blastholes. It was found that for the shallow-hole blasts used in most underground projects, the duration falls in the range from 2 to 5 ms. Based on this finding, YANG et al [39] investigated the seismic wave caused by only the rapid strain energy release with a theoretical model and then compared it with the explosion-induced seismic wave in terms of vibration characteristics. Because the duration of the strain energy release is much longer than the rise time of the explosion pressure, the frequency of the strain energy-related seismic wave is lower than that of the explosion-induced seismic wave. This causes the strain energy-related seismic wave to decay at a slower rate. Consequently, the magnitude of the strain energy-related seismic wave may exceed that of the explosion-induced seismic wave far from the blasthole. Additionally, due to its lower frequency, the strain energy-related seismic wave has greater potential to cause structural damage than does the explosion-induced seismic wave that has the same magnitude.

5 Discussion

The above numerical investigation results can provide some guidelines for the blasting design of deep rock mass excavation. Due to the suppression effect of in-situ stress on blast-induced rock fracture, the length of the crack growth is significantly reduced as the in-situ stress level increases. If the blasthole spacing commonly used in shallow rock mass blasting is used in deep rock masses that are subjected to high in-situ stress, the cracks may not spread completely throughout the zones between adjacent holes. This is unfavourable for rock fragmentation and excavation profile formation. Therefore, during the blasting of deep rock masses, it is recommended to properly reduce the blasthole spacing to increase rock fragmentation and the excavation profile quality. The crack growth during blast-induced rock fracture is related to the level of in-situ stress and many other factors, such as the rock properties, rock mass discontinuities, explosive type, charge structure and initiation mode. The reduction in the blasthole spacing during engineering practice needs to be determined through field tests. Under nonhydrostatic in-situ stress conditions, the longest cracks caused by blasting are mainly aligned in the direction of the maximum in-situ stress. This suggests that the blastholes should be arranged along the maximum in-situ stress orientation to facilitate crack connection between the blastholes. In deep tunnel blasting, the layout direction of the contour holes cannot be easily changed because it is limited by the position of the tunnel profile. However, the layout of the cutting holes, which are drilled in the innermost row and first detonated, can be adjusted according to the in-situ stress orientation. When the cutting holes in the same delay are arranged along the maximum in-situ stress orientation, the cracks between the adjacent holes are easier to connect, and thus a cavity more easily forms by cutting hole blasting. This is very important for tunnel blasting because the cavity will provide a new free surface for the subsequent hole blasts, and its formation is key to achieving the designed excavation footage.

The velocity of blasting vibration (blast-induced seismic waves) is a commonly used criterion for the assessment of structure damage under blast loading. Many experimental studies and engineering practices have shown that structural damage due to blasting vibration depends not only on the peak particle velocity (PPV) but also on the vibration frequency. The blasting vibration PPV and frequency predictions are important components in structure damage assessment and blasting design optimization. The above numerical investigations show that during blasting in deep rock masses, the transformation of explosion energy to seismic wave energy and the frequency of the seismic waves are

closely related to the in-situ stress level and orientation. The blasting vibration PPV is positively correlated with the seismic wave energy. Therefore, in the prediction of the PPV and frequency of the vibration caused by blasting of deep rock masses, the in-situ stress is an important factor that cannot be ignored. However, this regard has not attracted much attention in engineering practice. In comparison with the blasting of shallow rock masses with similar blasting parameters, the component of shear seismic waves is increased in deep rock mass blasting as a result of the asymmetrical release of rock strain energy. This is detrimental to the safety of the surrounding structures because shear seismic waves have a greater potential to cause damage to structures than compressive seismic waves.

Blast-induced rock fracture and seismic wave radiation in deep rock masses is a very complicated dynamic process. The work presented in this paper is a preliminary study, and some simplifications are made to facilitate the elucidation of the studied mechanisms. In practice, rock mass blasting involves three-dimensional explosive detonations, rock discontinuities, rock anisotropy and rock fragment movement. Clearly, the simplified plane model adopted in this study is limited in these aspects. Not with standing its limitations, the two-dimensional numerical investigation is still helpful for clarifying the radiation and energy transformation of blast-induced seismic waves in deep rock masses. Furthermore, there are several related issues that are worth researching, such as blast-induced seismic wave propagation in deep rock masses and the separation of explosion-induced seismic waves and rock strain energy-related components.

6 Conclusions

Rock masses at deep depths are subjected to high in-situ stress states. Blast-induced rock fractures and seismic wave radiation under in-situ stress conditions are numerically investigated by using the coupled SPH-FEM method. The results show that the in-situ stress state has an important effect on blast-induced rock fracture and seismic wave radiation outside the fractured zone. As the in-situ stress level increases, the size of the fractured zone shrinks significantly, and more explosion energy is transferred to the rock mass in the form of seismic waves. A smaller blast-induced fractured zone or seismic wave source zone under a higher in-situ stress corresponds to a higher seismic frequency at the elastic boundary. Under nonhydrostatic in-situ stress conditions, blast-induced cracks spread preferentially in the direction of the maximum in-situ stress. This anisotropic fracture pattern causes the energy density of explosion-induced seismic waves to be distributed nonuniformly around the blasthole. The highest seismic energy density occurs in the direction of the minimum in-situ stress, and the lowest density occurs in the direction of the maximum in-situ stress. Furthermore, during blasting in nonhydrostatic in-situ stress fields, S-waves are generated due to the asymmetrical release of rock strain energy during the anisotropic rock fracture. The amplitude of the S-waves increases with the in-situ stress level and is greatest in the minimum in-situ stress orientation.

Contributors

The overarching research goals were developed by YANG Jian-hua and YAO Chi. WU Ze-nan, SUN Wen-bin, and WANG Qiu-hui conducted the numerical simulations and analyzed the calculated results. The initial draft of the manuscript was written by YANG Jian-hua, WU Ze-nan, and YAO Chi. All authors replied to reviewers' comments and revised the final version.

Conflict of interest

YANG Jian-hua, WU Ze-nan, SUN Wen-bin, YAO Chi, and WANG Qiu-hui declare that they have no conflict of interest.

References

[1] FENG Xia-ting, YAO Zhi-bin, LI Shao-jun, et al. *In situ* observation of hard surrounding rock displacement at 2400 m-deep tunnels [J]. Rock Mechanics and Rock Engineering, 2018, 51(3): 873–892. DOI: 10.1007/s00603-017-1371-3.

[2] WAGNER H. Deep mining: A rock engineering challenge [J]. Rock Mechanics and Rock Engineering, 2019, 52(5): 1417–1446. DOI: 10.1007/s00603-019-01799-4.

[3] HUANG Fu, ZHANG Min, JIANG Zhen. Collapse mode of rock mass induced by a concealed Karst cave above a deep cavity [J]. Journal of Central South University, 2019, 26(7):

1747−1754. DOI: 10.1007/s11771-019-4130-7.

[4] SIREN T, KANTIA P, RINNE M. Considerations and observations of stress-induced and construction-induced excavation damage zone in crystalline rock [J]. International Journal of Rock Mechanics and Mining Sciences, 2015, 73: 165−174. DOI: 10.1016/j.ijrmms.2014.11.001.

[5] LUO Yong, GONG Feng-qiang, LI Xi-bing, et al. Experimental simulation investigation of influence of depth on spalling characteristics in circular hard rock tunnel [J]. Journal of Central South University, 2020, 27(3): 891−910. DOI: 10.1007/s11771-020-4339-5.

[6] KUTTER H K, FAIRHURST C. On the fracture process in blasting [J]. International Journal of Rock Mechanics and Mining Sciences & Geomechanics Abstracts, 1971, 8(3): 181−202. DOI: 10.1016/0148-9062(71)90018-0.

[7] YANG Li-yun, DING Chen-xi. Fracture mechanism due to blast-imposed loading under high static stress conditions [J]. International Journal of Rock Mechanics and Mining Sciences, 2018, 107: 150−158. DOI: 10.1016/j.ijrmms.2018.04.039.

[8] QIU Peng, YUE Zhong-wen, JU Yang, et al. Characterizing dynamic crack-tip stress distribution and evolution under blast gases and reflected stress waves by caustics method [J]. Theoretical and Applied Fracture Mechanics, 2020, 108: 102632. DOI: 10.1016/j.tafmec.2020.102632.

[9] QIU Peng, YUE Zhong-wen, YANG Ren-shu, et al. Effects of vertical and horizontal reflected blast stress waves on running cracks by caustics method [J]. Engineering Fracture Mechanics, 2019, 212: 164−179. DOI: 10.1016/j.engfracmech.2019.03.018.

[10] HE Cheng-long, YANG Jun. Dynamic crack propagation of granite subjected to biaxial confining pressure and blast loading [J]. Latin American Journal of Solids and Structures, 2018, 15(6): e45. DOI: 10.1590/1679-78254463.

[11] MA G W, AN X M. Numerical simulation of blasting-induced rock fractures [J]. International Journal of Rock Mechanics and Mining Sciences, 2008, 45(6): 966−975. DOI: 10.1016/j.ijrmms.2007.12.002.

[12] YILMAZ O, UNLU T. Three dimensional numerical rock damage analysis under blasting load [J]. Tunnelling and Underground Space Technology, 2013, 38: 266−278. DOI: 10.1016/j.tust.2013.07.007.

[13] PENG Jian-yu, ZHANG Feng-peng, DU Chuan, et al. Effects of confining pressure on crater blasting in rock-like materials under electric explosion load [J]. International Journal of Impact Engineering, 2020, 139: 103534. DOI: 10.1016/j.ijimpeng.2020.103534.

[14] WENG Lei, WU Qiu-hong, ZHAO Yan-lin, et al. Dynamic response and failure of rock in initial gradient stress field under stress wave loading [J]. Journal of Central South University, 2020, 27(3): 963−972. DOI: 10.1007/s11771-020-4344-8.

[15] DAI Jun, QIAN Qi-hu. Break blasting parameters for driving a roadway in rock with high residual stress [J]. Explosion and Shock Waves, 2007, 27(3): 272−277. (in Chinese)

[16] HUSTRULID W A. Blasting principles for open pit mining [M]. Brookfield: A. A. Balkema Publishers, 1999.

[17] BLAIR D P, JIANG J J. Surface vibrations due to a vertical column of explosive [J]. International Journal of Rock Mechanics and Mining Sciences & Geomechanics Abstracts, 1995, 32(2): 149−154. DOI: 10.1016/0148-9062(94)00036-3.

[18] CHEN Shi-hai, WU Jian, ZHANG Zi-hua. Blasting vibration characteristics and PPV calculation formula considering cylindrical charge length [J]. Environmental Earth Sciences, 2017, 76(20): 1−12. DOI: 10.1007/s12665-017-7027-5.

[19] AHN J K, PARK D. Prediction of near-field wave attenuation due to a spherical blast source [J]. Rock Mechanics and Rock Engineering, 2017, 50(11): 3085−3099. DOI: 10.1007/s00603-017-1274-3.

[20] SHIN J H, MOON H G, CHAE S E. Effect of blast-induced vibration on existing tunnels in soft rocks [J]. Tunnelling and Underground Space Technology, 2011, 26(1): 51−61. DOI: 10.1016/j.tust.2010.05.004.

[21] YANG Jian-hua, CAI Ji-yong, YAO Chi, et al. Comparative study of tunnel blast-induced vibration on tunnel surfaces and inside surrounding rock [J]. Rock Mechanics and Rock Engineering, 2019, 52(11): 4747 − 4761. DOI: 10.1007/s00603-019-01875-9.

[22] KONESHWARAN S, THAMBIRATNAM D P, GALLAGE C. Blast response of segmented bored tunnel using coupled SPH-FE method [J]. Structures, 2015, 2: 58 − 71. DOI: 10.1016/j.istruc.2015.02.001.

[23] LU Yong, WANG Zhong-qi, CHONG Ka-ren. A comparative study of buried structure in soil subjected to blast load using 2D and 3D numerical simulations [J]. Soil Dynamics and Earthquake Engineering, 2005, 25(4): 275 − 288. DOI: 10.1016/j.soildyn.2005.02.007.

[24] JOHNSON G R, HOLMQUIST T J. An improved computational constitutive model for brittle materials [J]. AIP Conference Proceedings, 1994, 309(1): 981−984. DOI: 10.1063/1.46199.

[25] AI H A, AHRENS T J. Simulation of dynamic response of granite: A numerical approach of shock-induced damage beneath impact craters [J]. International Journal of Impact Engineering, 2006, 33(1 − 12): 1 − 10. DOI: 10.1016/j.ijimpeng.2006.09.046.

[26] DEHGHAN B M M, MOHANTY B. Numerical simulation of stress wave induced fractures in rock [J]. International Journal of Impact Engineering, 2012, 40−41: 16−25. DOI: 10.1016/j.ijimpeng.2011.08.010.

[27] BLAIR D P. The free surface influence on blast vibration [J]. International Journal of Rock Mechanics and Mining Sciences, 2015, 77: 182−191. DOI: 10.1016/j.ijrmms.2015.04.006.

[28] ESEN S, ONEDERRA I, BILGIN H A. Modelling the size of the crushed zone around a blasthole [J]. International Journal of Rock Mechanics and Mining Sciences, 2003, 40(4): 485−495. DOI: 10.1016/S1365-1609(03)00018-2.

[29] BROWN E T, HOEK E. Underground excavations in rock [M]. London: Institution of Mining and Metallurgy, 1980.

[30] JUNG W J, UTAGAWA M, OGATA Y, et al. Effects of rock pressure on crack generation during tunnel blasting [J]. Kayaku Gakkaishi/Journal of the Japan Explosives Society, 2001, 62(3): 138−146.

[31] ACHENBACH J D. Wave propagation in elastic solids [M]. Amsterdam: Elsevier, 1975.

[32] TRIVIÑO L F, MOHANTY B, MILKEREIT B. Seismic waveforms from explosive sources located in boreholes and

initiated in different directions [J]. Journal of Applied Geophysics, 2012, 87: 81−93. DOI: 10.1016/j.jappgeo.2012.09.004.

[33] JOHNSTON D H, TOKSÖZ M N. Ultrasonic P and S wave attenuation in dry and saturated rocks under pressure [J]. Journal of Geophysical Research: Solid Earth, 1980, 85(B2): 925−936. DOI: 10.1029/JB085iB02p00925.

[34] VOZNESENSKII A S, KUTKIN Y O, KRASILOV M N, et al. The influence of the stress state type and scale factor on the relationship between the acoustic quality factor and the residual strength of gypsum rocks in fatigue tests [J]. International Journal of Fatigue, 2016, 84: 53 − 58. DOI: 10.1016/j.ijfatigue.2015.11.016.

[35] CAO Wen-zhuo, LI Xi-bing, TAO Ming, et al. Vibrations induced by high initial stress release during underground excavations [J]. Tunnelling and Underground Space Technology, 2016, 53: 78 − 95. DOI: 10.1016/j.tust.2016.01.017.

[36] YANG J H, JIANG Q H, ZHANG Q B, et al. Dynamic stress adjustment and rock damage during blasting excavation in a deep-buried circular tunnel [J]. Tunnelling and Underground Space Technology, 2018, 71: 591 − 604. DOI: 10.1016/j.tust.2017.10.010.

[37] ARCHAMBEAU C B. General theory of elastodynamic source fields [J]. Reviews of Geophysics, 1968, 6(3): 241. DOI: 10.1029/rg006i003p00241.

[38] LU Wen-bo, YANG Jian-hua, YAN Peng, et al. Dynamic response of rock mass induced by the transient release of in situ stress [J]. International Journal of Rock Mechanics and Mining Sciences, 2012, 53: 129 − 141. DOI: 10.1016/j.ijrmms.2012.05.001.

[39] YANG Jian-hua, LU Wen-bo, JIANG Qing-hui, et al. A study on the vibration frequency of blasting excavation in highly stressed rock masses [J]. Rock Mechanics and Rock Engineering, 2016, 49(7): 2825−2843. DOI: 10.1007/s00603-016-0964-6.

(Edited by ZHENG Yu-tong)

中文导读

深部岩体爆破爆炸地震波辐射模式与能量特性数值模拟研究

摘要：对于深部岩体爆破，普遍认为地应力的存在将改变爆生裂纹的传播过程并最终影响岩体爆破开裂区的分布，但对于地应力作用下岩体爆破开裂区形态改变对爆炸地震波辐射模式的影响，目前还鲜有研究报道。本文采用SPH-FEM耦合数值模拟方法，研究了地应力对岩体爆破开裂及爆炸地震波辐射模式和能量特性的影响。结果表明，在地应力作用下岩体爆破开裂区形态改变对爆炸地震波能量及组成成分具有显著的影响；随着地应力水平的提高，岩体爆破开裂区范围缩小，更多的爆炸能转化为地震波能量，地应力作用下爆破开裂区(即爆炸地震波产生区)范围缩小导致地震波的频率升高；在非静水地应力条件下，沿最小主应力方向传播的爆生裂纹更易受到地应力的抑制，因此沿该方向传播的地震波的能量密度更高；在非静水地应力条件下各向异性的岩体爆破开裂模式导致岩体应变能非对称地快速释放，从而在岩体中诱发剪切波。

关键词：爆破；地应力；地震波；岩体开裂；SPH-FEM